Editors' Suggestion

Spatial addressing of qubits in a dispersive waveguide

Maximilian Zanner,[1,2,*,†] Romain Albert,[1,2,3,*,‡] Eric I. Rosenthal,[4] Silvia Casulleras,[1,5] Ian Yang,[1,2] Christian M.F. Schneider,[1,2] Oriol Romero-Isart,[1,5,6,7] and Gerhard Kirchmair[1,2]

[1] *Institute for Quantum Optics and Quantum Information, Austrian Academy of Sciences, 6020 Innsbruck, Austria*
[2] *University of Innsbruck, Institute for Experimental Physics, 6020 Innsbruck, Austria*
[3] *Silent Waves, 69-73 rue Félix Esclangon, 38000 Grenoble Cedex 09, France*
[4] *E.L. Ginzton Laboratory, Stanford University, Stanford, California 94305, USA*
[5] *Institute for Theoretical Physics, University of Innsbruck, 6020 Innsbruck, Austria*
[6] *ICFO—Institut de Ciencies Fotoniques, Barcelona Institute of Science and Technology, 08860 Castelldefels, Barcelona, Spain*
[7] *ICREA, Passeig Lluis Companys 23, 08010 Barcelona, Barcelona, Spain*

(Received 8 August 2024; revised 27 April 2025; accepted 27 June 2025; published 28 July 2025)

Waveguide quantum electrodynamics—the study of atomic systems interacting with propagating electromagnetic fields—is a powerful platform for understanding the complex interplay between light and matter. Qubit control is an indispensable tool in this field, and most experiments thus far have used narrowband control pulses to interact with qubits at specific frequencies. Dynamics can change significantly with fast, broadband pulses, since waveguide properties such as dispersion affect the pulse evolution and its impact on the qubit. Here we use dispersion to achieve spatial addressing of superconducting qubits separated by a subwavelength distance within a microwave waveguide. This approach relies on a self-focusing effect to create a position-dependent interaction between a chirped pulse and an individual qubit. This method emphasizes the importance of dispersion in the design and analysis of quantum experiments, and offers avenues for the rapid control of quantum states.

DOI: 10.1103/np2t-48rm

I. INTRODUCTION

A propagating wave is said to disperse if its envelope changes over time. Dispersion arises either due to the material properties of the medium [1] or from the geometric confinement of the propagating field [2,3]. Understanding the propagation of electromagnetic waves in different media, including the effects of dispersion, plays a central role in modern information technology. This understanding is essential both in the classical regime, such as in telecommunications (e.g., fiber optic cables), and in the quantum regime, where single photons must be routed and controlled with high fidelity. Consequently, dispersion is highly relevant to the field of waveguide quantum electrodynamics (QED), which investigates fundamental light-matter interactions and quantum protocols involving propagating waves [4,5].

Waveguide QED using superconducting circuits has been successful in investigating quantum phenomena where quantum emitters interact with a propagating microwave field. Landmark experiments include the first realization of strong coupling between a superconducting qubit and a one-dimensional transmission line [6], the creation of super-radiant and subradiant states formed by multiple emitters [7,8], the demonstration of single-photon routers [9], and the achievement of multiphoton entangled states [10] as well as interacting bound states [11]. Other significant achievements include the entangling of distant quantum systems to perform Bell tests [12], the creation of giant atoms using self-interference [13], and the realization of chiral interactions and unidirectional photon emitters [14–16].

In all these experiments, quantum emitters interact with waveguide photons within a narrow bandwidth, allowing the impact of dispersion to be ignored. However, dispersion significantly affects the temporal shape of short, wideband wave packets in quantum communication protocols, similarly to its impact in classical communication technology. Consequently, understanding wave-packet evolution

*These two authors contributed equally.
†Contact author: zanner.maximilian@gmail.com
‡Contact author: romain@silent-waves.com

Published by the American Physical Society under the terms of the Creative Commons Attribution 4.0 International license. Further distribution of this work must maintain attribution to the author(s) and the published article's title, journal citation, and DOI.

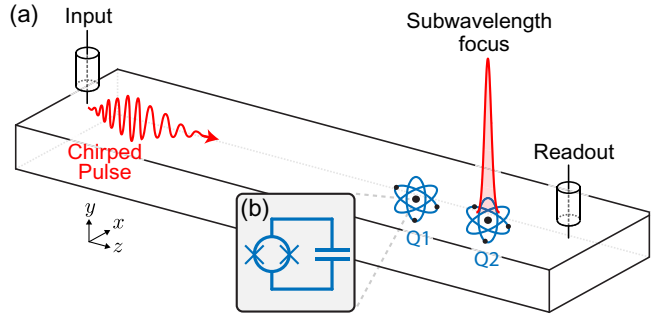


FIG. 1. Self-focusing pulses for fast, selective control of quantum emitters. (a) A chirped pulse travels along a dispersive waveguide. Dispersion causes different frequency components to propagate at different group velocities, such that a broadband input pulse may be designed to focus at a specific position. (b) This pulse can be used for quantum control. Here we study the interplay between this pulse and two superconducting transmon qubits (Q1 and Q2).

due to dispersion and appropriately tailoring control pulses is crucial for high-fidelity gate operations between distant quantum nodes and the creation of multiphoton entangled states.

Rather than solely being a detrimental effect that must be corrected for, dispersion opens up new possibilities to engineer light-matter interactions with exotic properties [11,17–19]. For example, dispersion enables the propagation of self-focusing pulses, [20], demonstrated in pulse compression schemes [1] that have revolutionized the field of attosecond physics [21]. Focused pulses tailored via dispersion also offer novel avenues for the control of quantum systems, including recent theoretical work on the use of dispersion to address individual quantum emitters [22].

Here we use dispersion to create fast, localized microwave pulses to selectively control superconducting transmon qubits within a waveguide. Specifically, we demonstrate this technique using the nonlinear dispersion around the cutoff frequency of a microwave waveguide, where the group velocity has a strong spectral dependence. By shaping the phase and amplitude of a chirped microwave pulse within a bandwidth of several gigahertz, we induce a self-focusing effect that allows us to individually address two transmons, denoted as Q1 and Q2, which are separated by a subwavelength distance (Fig. 1). This experiment demonstrates a control scheme for qubits embedded in dispersive media based on the position-dependent interaction between the pulse and the qubits. This method could have wide applicability to quantum systems for which local qubit control is difficult to engineer.

II. A SELF-FOCUSING CHIRPED PULSE

Our system consists of a rectangular microwave waveguide that allows propagation of transverse electric (TE) and transverse magnetic waves [2]. Fields within the waveguide propagate via the dispersion relation

$$\omega(k) = c\sqrt{k^2 + k_c^2} \tag{1}$$

and have group velocity $v_g = \partial\omega(k)/\partial k$, where $k = 2\pi/\lambda$ is the wave vector (with λ the wavelength) and c is the speed of light in the waveguide material (vacuum). The cutoff wave vector $k_c = 2\pi f_c/c$ is determined by the geometry of the waveguide boundaries. Below f_c, light does not propagate along the waveguide, while above f_c, the group velocity increases from zero and asymptotically reaches c in the high-frequency limit. We excite only the lowest-order TE mode, which has a cutoff frequency $f_c = 6.56$ GHz; see Appendixes D and E for details on the waveguide geometry and coupling elements.

The individual spectral components of a pulse propagate at different velocities due to dispersion. This means a focused pulse will disperse and, conversely, a chirped pulse can be tailored to focus at a given position. We first demonstrate this focusing effect in a room-temperature experiment (Fig. 2). Using a 65×10^9 samples/s arbitrary waveform generator (AWG), we generate a wave packet whose time-dependent field at the focal point is given by

$$E_f(t) = E_0 \int_0^\infty \mathrm{d}k\, \tilde{E}(k) \cos(\omega(k)t), \tag{2}$$

$$\tilde{E}(k) = \exp(-\frac{1}{2}\sigma_f^2(k-k_0)^2), \tag{3}$$

where k_0 is the central wave vector, σ_f is the focal spot size, and E_0 is an arbitrary amplitude. To optimize self-focusing and minimize reflections, the electric field components in reciprocal space $\tilde{E}(k)$ are chosen to be a Gaussian centered at $k = k_0$, where k_0 is the wave number associated with a center frequency f_0 of 7.2 GHz and with a spatial width σ_f of 3.5 cm [Fig. 2(c)].

Equation (2) can be backpropagated to compute the electric field at an arbitrary location z along the waveguide:

$$E(t,z) = \int_{-\infty}^{\infty} \mathrm{d}t' h(t-t',z) E_f(t'), \tag{4}$$

where $h(t,z) = 1/2\pi \int_{-\infty}^{\infty} \mathrm{d}\omega e^{-i(\omega t - kz)}$ is the impulse response that follows from the convolution theorem [23] and $k = \sqrt{\omega^2 - \omega_c^2}/c$ is given by the dispersion relation. We may thus compute the delocalized input pulse $E(t, z = -d_f)$. This has the same spectral density as shown in Fig. 2(c) but is chirped (slowly propagating components are input ahead of faster ones) such that all components constructively interfere at the focal point d_f.

In the experiment corresponding to Fig. 2(d), we compare a defocused input to the electric field at the focal point $d_f = 1.03$ m. This field is measured with a weakly coupled

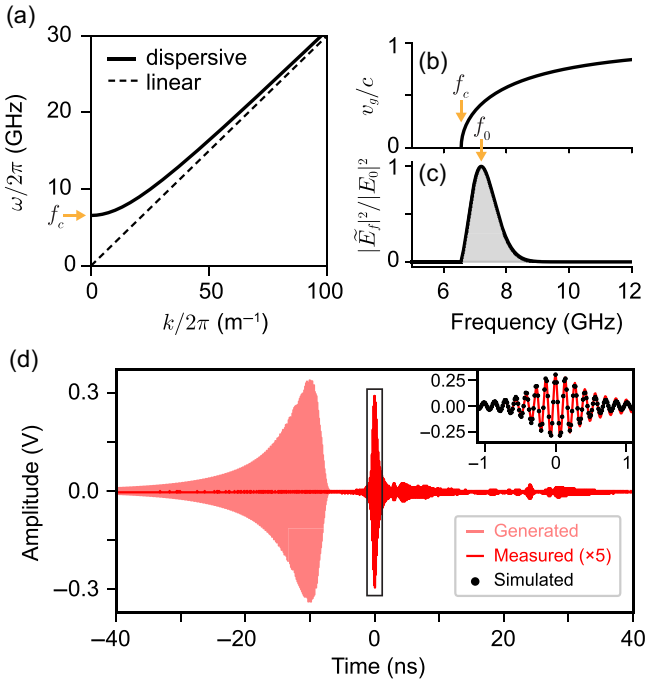


FIG. 2. A self-focusing pulse. (a) The dispersion relation $\omega(k)$, which exhibits a low-frequency cutoff $f_c = 6.56\,\mathrm{GHz}$ below which light does not propagate. Linear dispersion is shown for comparison (dashed line) [see Eq. (1)]. (b) Group velocity $v_g = \partial\omega(k)/\partial k$ vs frequency. In the high-frequency limit, the group velocity approaches c, the speed of light in the waveguide material (vacuum). (c) Normalized power spectral density of the pulse described in Eq. (3), which has a center frequency f_0 of 7.2 GHz. (d) A chirped version of this pulse is generated at the waveguide input (light red), and is measured at a focal point $d_f = 1.03\,\mathrm{m}$ from the waveguide input (darker red). In excellent agreement with theory, the pulse is compressed from greater than 10 ns in duration to approximately 0.5 ns in duration (inset). Time $t = 0$ corresponds to the pulse arrival time; signal collected significantly later is due to reflection at the waveguide couplers.

antenna connected to an oscilloscope with 12.5 GHz analog bandwidth (see Appendix D for experimental details). Measurements show clear agreement with the waveform expected by Eq. (2). Ripples that occur after the focal time are due to reflection at the waveguide boundaries. Comparison of the temporal full width at half maximum (FWHM) of the pulse at the output of the generator $\sigma_{\mathrm{AWG}} = 10\,\mathrm{ns}$ with the temporal FWHM of the pulse at the focal point $\sigma_f < 1\,\mathrm{ns}$ shows pulse compression by more than a factor of 10. This conclusively demonstrates self-focusing of a chirped pulse.

III. QUANTUM CONTROL

We now use this self-focused pulse to demonstrate selective qubit control (Fig. 3). Treating the qubit as an ideal two-level system, we model its dynamics as a Landau-Zener process in which the qubit eigenenergies exhibit an avoided crossing with an energy gap $g(t,z)$ that is proportional to the field amplitude [22]. For a pulse with electric field $E(t,z) = A(t,z)\exp(i\phi(t,z))$, where $A(z,t)$ are $\phi(t,z)$ are its instantaneous amplitude and phase, respectively, the pulse-qubit dynamics are described by the Hamiltonian

$$\frac{\hat{H}_{\mathrm{LZ}}}{\hbar} = \Delta(t,z)\hat{\sigma}_z + \frac{g(t,z)}{2}\left(\hat{\sigma}_+ + \hat{\sigma}_-\right) \tag{5}$$

in the frame obtained by our applying the unitary transformation $\hat{U} = e^{-i\phi(t,z)\hat{\sigma}_z/2}$. Here $\Delta(t,z) = \omega_q - \partial_t\phi(t,z)$, where $\partial_t\phi(t,z)$ is the instantaneous frequency of the pulse, and $g(t,z) = d_{eg}A(t,z)$ is the Rabi coupling, with d_{eg} the qubit's electric dipole moment. Finally, $\hat{\sigma}_z$, $\hat{\sigma}_+$, and $\hat{\sigma}_-$ are standard qubit operators. See Appendixes A and F for more details, and Ref. [22] for a discussion of how dynamics are modified by a transmon's higher energy levels.

When a qubit in its ground state lies within the spot size σ_f of the pulse, it is excited and subsequently de-excited as the pulse passes [22]. A qubit located out of focus, however, transitions to the excited state and remains excited after the pulse interaction. This behavior arises from the interplay between the pulse's instantaneous amplitude and the qubit's detuning. So after the pulse had passed, all qubits except the one at the focal point are excited. This state could, in principle, be inverted by one sending an additional unfocused pulse that flips the state of all qubits such that only a single one remains excited.

We experimentally test this behavior in the waveguide QED experiment corresponding to Fig. 3. Two superconducting transmon qubits (Q1 and Q2) are embedded in a dispersive microwave waveguide [2,24]. The qubits are spaced $d_z \approx 5\,\mathrm{cm}$ apart, which corresponds to approximately half a wavelength at the pulse center frequency $f_0 = 7.2\,\mathrm{GHz}$. With the use of an external magnetic coil, each qubit can be independently tuned in or out of the waveguide passband, such that their transition frequencies f_{Q1} and f_{Q2} can match f_0. Each qubit is coupled to a readout resonator, allowing measurement of its state (see Fig. 13 in Appendix E and Appendix F for a readout calibration).

We first show that the population of a single qubit can be controlled by its interaction with the chirped pulse. To do so, one qubit is tuned to 7.2 GHz, while the other is tuned below the waveguide cutoff frequency. We send a chirped pulse of spot size $\sigma_f = 3.5\,\mathrm{cm}$ and vary its focal point d_f after calibrating its amplitude for maximum interaction (see Appendix C). In Fig. 3(c) we show the resulting ground state population $P_{|g\rangle}$ of each qubit measured immediately after interaction with this pulse, which is peaked around the position at which the focal distance of the pulse coincides with the position of the qubit.

Next we demonstrate spatial addressing in a two-qubit system. To do so, we tune both qubits to 7.28 GHz and

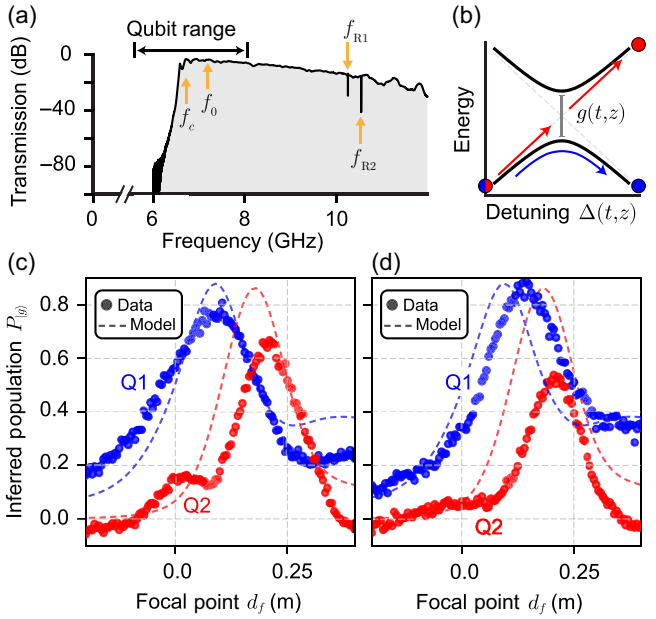


FIG. 3. Spatial addressing of qubits. (a) Transmission measured through the waveguide showing a cutoff frequency f_c of 6.56 GHz, below the pulse center frequency $f_0 = 7.2$ GHz. Resonances at $f_{R1} = 10.25$ GHz and $f_{R2} = 10.55$ GHz are for the readout resonators (see Appendix D). Q1 and Q2 are positioned at approximately 15 cm and 20 cm from the waveguide input, respectively. (b) Eigenenergies of the Landau-Zener process describing the dynamical interaction between the qubit and the chirped pulse. The instantaneous energy gap $g(z,t)$ and detuning $\Delta(z,t)$ are functions of the pulse electric field $E(z,t)$. The qubit remains in the lower energy branch only if it is centered at the pulse's focal point (blue circles and blue arrows) and otherwise transitions to the excited state (red circles and red arrows). (c) Inferred probability of measuring Q1 or Q2 in the ground state after the interaction with a chirped pulse while the other qubit is tuned below the waveguide cutoff to limit its interaction. (d) Interaction when both qubits are tuned to the same frequency $f_{Q1} = f_{Q2} = f_0$. In (c),(d), the pulse amplitude has been optimized to maximize adressability, and is compared with a simulation that includes reflection at the waveguide output (see Appendix B).

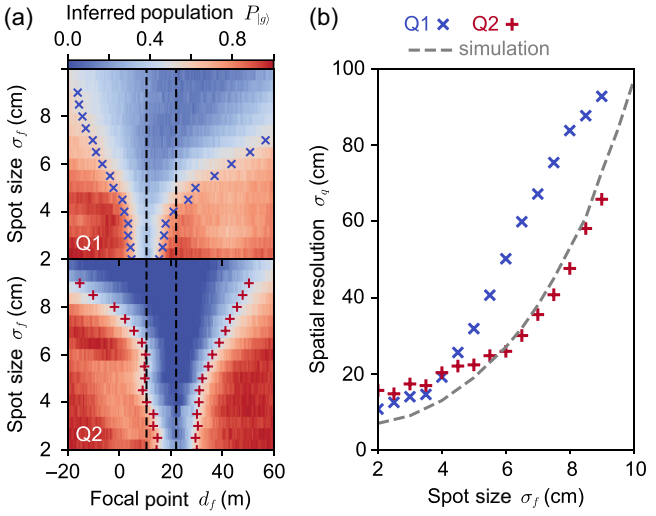


FIG. 4. Spatial resolution of the qubit addressability. (a) Inferred ground state population $P_{|g\rangle}$ of each qubit (Q1 or Q2) as a function of the chirped pulse's focal point d_f and its spot size σ_f. For each panel only the frequency of the corresponding qubit is tuned inside the waveguide band (top, Q1; bottom, Q2). The red and blue crosses indicate the FWHM of the spatial resolution σ_q, extracted from the data. As the spot size σ_f decreases from 0.1 to 0.02 m, the spatial resolution σ_q is reduced, reaching a minimum value of approximately 15 cm. Dashed black lines are included at the positions of optimal effect, 10.6 and 22.1 cm, as a guide for the eye. (b) Measured spatial resolution σ_q as a function of the spot size σ_f of the pulse, compared with the simulation of an ideal pulse interacting with the qubit (gray).

measure the ground state population of both qubits immediately after a chirped pulse [Fig. 3(d)]. The results demonstrate that the pulse-qubit interaction is able to selectively address the qubits separately even when they are tuned to the same frequency, in a manner that is qualitatively similar to that in the single-qubit experiment as shown in Fig. 3(b). Note that in this experiment photon-mediated qubit-qubit interactions can be ignored since these are governed by the $\Gamma_q/2\pi \approx 30$ kHz strength of qubit coupling to the waveguide [8,25], an interaction that occurs over a much longer timescale than the approximately 100 ns chirped pulse.

These measurements demonstrate the ability to selectively address individual qubits spaced within a wavelength distance. In both the single-qubit case and the two-qubit case, distortion and reflection of the pulse ultimately result in unwanted qubit dynamics, limiting the state preparation fidelity and spatial resolution. To qualitatively understand this, the measurements in Fig. 3 are compared with a model that includes a broadband reflection coefficient of 10% at the waveguide output (see Appendix B for details).

Finally, we demonstrate control over the spatial resolution associated with the ability to address our qubit by varying the spot size σ_f of the focusing pulse. To quantify this effect, we define the pulse's spatial resolution σ_q as the FWHM of the measured ground state population $P_{|g\rangle}$, as a function of a variable focal point d_f. This is shown by the horizontal distance between the markers in Fig. 4(a). Spatial resolution is plotted in Fig. 4(b) as a function of spot size. At large spot sizes we see a weak dependence of σ_q on the focal point, as expected for a conventional waveguide QED system. When σ_f is decreased, however, the population in the ground state $P_{|g\rangle}$ shows a stronger dependence on the focal point, effectively reducing σ_q. For small values of σ_f, the spatial resolution saturates to $\sigma_q \approx 15$ cm, which is limited by the dispersion relation and other experimental limitations, such as reflection off the waveguide boundaries (see Appendix B).

IV. CONCLUSION

Our findings represent realization of position-dependent qubit addressing using self-compressing pulses. In contrast to conventional quantum control, where the pulse energy determines the final qubit state, our experiment is a study of the interaction between qubits and broadband pulses. Doing so, we selectively address one qubit or two qubits with a minimal spatial resolution $\sigma_q \approx 15$ cm, near subwavelength, and limited by the dispersion of the waveguide with a finite speed of light and experimental imperfections. Analogous to classical high-speed communication where dispersion has to be taken into account, our results emphasize the important role of dispersion for quantum physics experiments when broadband pulses are used.

We expect that modifications such as optimizing the impedance matching of the waveguide–coaxial-cable adapters around the qubit frequencies, increasing the qubit coherence by operating at a flux sweet spot, and increasing the qubit-waveguide coupling will increase the preparation fidelity and the spatial resolution. We also emphasize that other quantum systems that use optical fibers do not suffer from reflections as the return loss can be reduced below −40 dB. In addition, the current experiment shows limitations caused by the small anharmonicity of the transmon qubits used, which leads to the driving of multiphoton transitions and leakage out of the qubit ground and excited states (see Appendix F and Ref. [22]). This problem can be avoided by the use of other types of qubit, e.g., a fluxonium [26], which typically has a greater anharmonicity.

The demonstrated technique is general to quantum communication and quantum simulation experiments where multiple qubits are coupled to a waveguide and local control cannot be directly engineered. Locally exciting a chain of qubits without the need to physically adapt the experimental architecture provides a powerful tool to allow state preparation in Ising-physics simulations [27,28] or to drive multiqubit dark states [8]. Finally, this technique can be applied to other types of atomic systems such as solid-state spin qubits (e.g., the nitrogen-vacancy center in diamond), whose point-dipole nature makes spatially close qubits difficult to individually address with microwave pulses [29] or atoms coupled to optical fibers [30], where spatial addressing is very difficult.

ACKNOWLEDGMENTS

We thank Carlos Gonzalez-Ballestero for valuable input and discussions about the self-focusing theory. We thank Andreas Strasser for fabricating the waveguide. M.Z. acknowledges funding by the European Research Council under the European Union's Horizon 2020 research and innovation program (Grant No. 714235). This research was funded in part by the Austrian Science Fund (FWF) (Grant DOI 10.55776/W1259 and Grant DOI 10.55776/F71). E.I.R. acknowledges support from an appointment to the Intelligence Community Postdoctoral Research Fellowship Program at Stanford University administered by Oak Ridge Institute for Science and Education through an interagency agreement between the U.S. Department of Energy and the Office of the Director of National Intelligence.

G.K., M.Z., and R.A. conceived and designed the experiment. M.Z. simulated and M.Z., C.M.F.S., and I.Y. fabricated the devices. E.I.R., M.Z., and R.A. conducted the measurements. M.Z. and R.A. analyzed the data. O.R.-I., R.A., and S.C. developed the theoretical model. E.I.R., G.K., M.Z., and R.A. wrote the manuscript. All authors discussed the results and contributed to the writing of the manuscript.

The authors declare that they have no competing interests.

DATA AVAILABILITY

The data that support the plots within this paper and the appendixes are available via a permanent, public repository [31].

APPENDIX A: THEORY

In this appendix, we describe the impact of dispersion on the propagation of a chirped pulse traveling inside a rectangular waveguide and its interaction with a single quantum emitter, following Ref. [22]. We write the classical electric field associated with a Gaussian pulse in k-vector space:

$$\tilde{E}(k) \propto \exp\left(-\frac{\sigma_f^2(k-k_0)^2}{2}\right), \tag{A1}$$

where σ_f is the spot size and k_0 is the central k vector of the pulse. To perform the experiment, pulse frequencies near the cutoff of the rectangular waveguide, which are not well coupled to the waveguide [see Fig. 1(a)], are removed. Moreover, these frequencies travel very slowly and thus create long AWG waveforms, causing numerical instability. To avoid this, the pulse definition in Eq. (A1) is modified with a smooth high-pass filter; that is,

$$\tilde{E}_2(k) \propto \exp\left(-\frac{\sigma_f^2(k-k_0)^2}{2}\right)\exp\left(\frac{-0.01\times k_c^2}{k^2}\right), \tag{A2}$$

where the high-pass filter has a 3 dB point of 6.605 GHz (compared with 6.557 GHz for the waveguide cutoff) and does not significantly change the shape of the pulse.

The temporal behavior of the pulse at a given position $z = d_f$ can then be computed with use of the dispersion

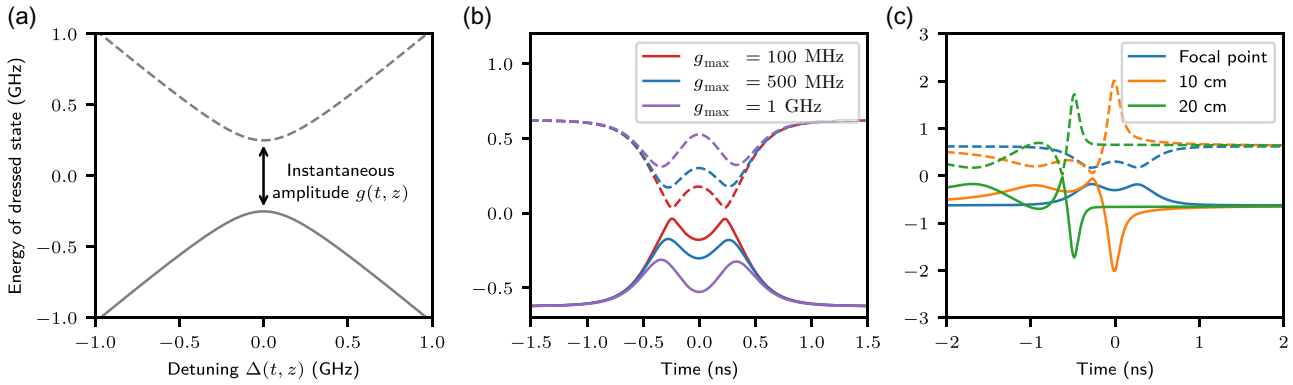


FIG. 5. Landau-Zener explanation of the qubit dynamics. (a) Energy of the dressed states of the qubit in the Landau-Zener picture as a function of the detuning and instantaneous Rabi coupling amplitude. (b) Energy of the dressed states as a function of time at the focal point for different pulse amplitudes [$g_{\max} = \max(g(t, z_f))$]. (c) Energy of the dressed states at the focal point, and at 10 and 20 cm before the focal point.

relation $\omega(k)$ of the waveguide as

$$E_f(t) = E_0 \,\mathrm{Re}\left[\int_0^\infty \mathrm{d}k \tilde{E}_2(k) \exp\left(i\omega(k)t\right)\right], \qquad \text{(A3)}$$

where $\omega(k) = c\sqrt{k^2 + k_c^2}$, where k_c is the cutoff k vector of the rectangular waveguide, and E_0 is the amplitude of the pulse. Here the cutoff k vector is linked to the cutoff frequency of the rectangular waveguide through the relation $k_c = \omega_c/c$, where c is the speed of light in the

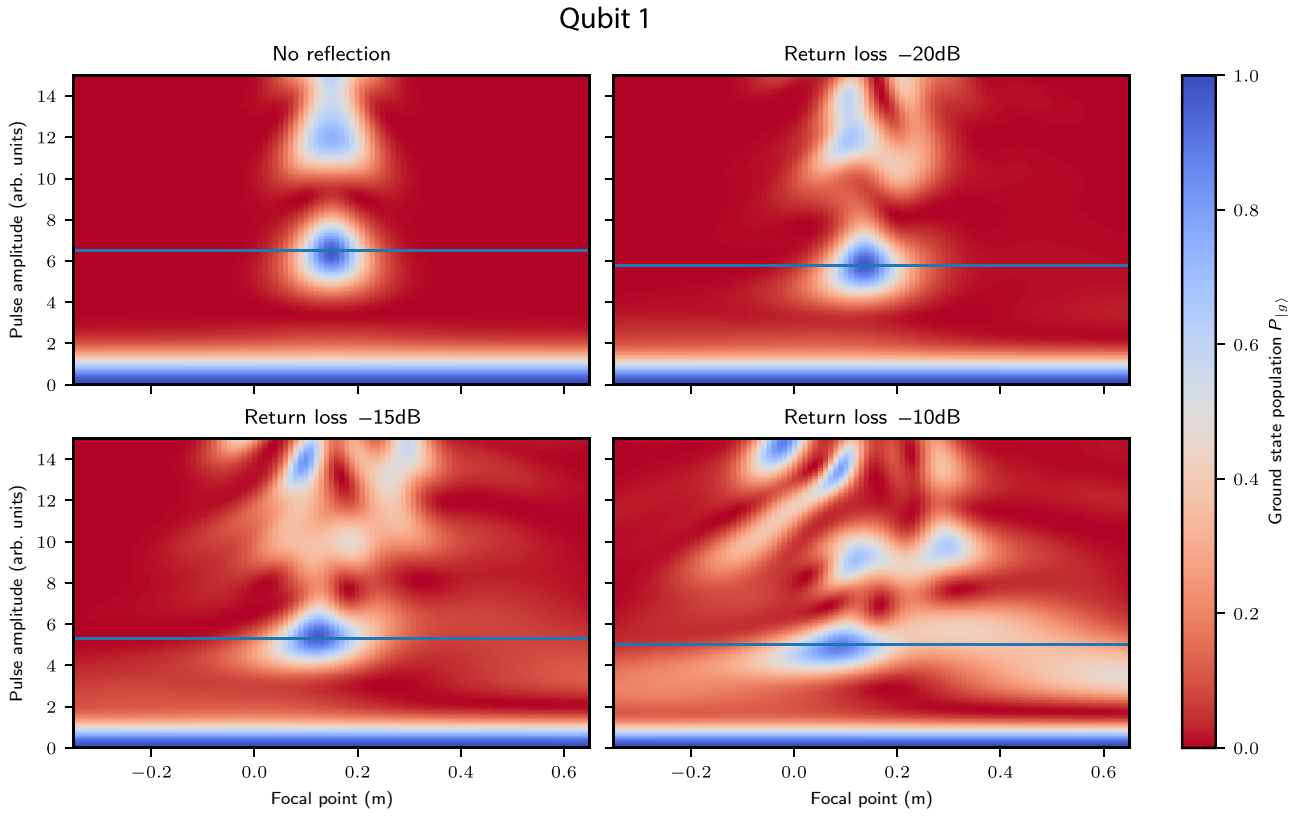


FIG. 6. Ground state population vs return loss for Q1. Simulated ground state population for a transmon at a frequency of 7.2 GHz and an anharmonicity of 420 MHz after interacting with a pulse with a focal point $z = 0$ m and a spot size of 3.5 cm. The different panels show different amplitudes of the parasitic reflection. The reflection considered is constant for all frequencies, and the source of the reflection is 10 cm from the qubit.

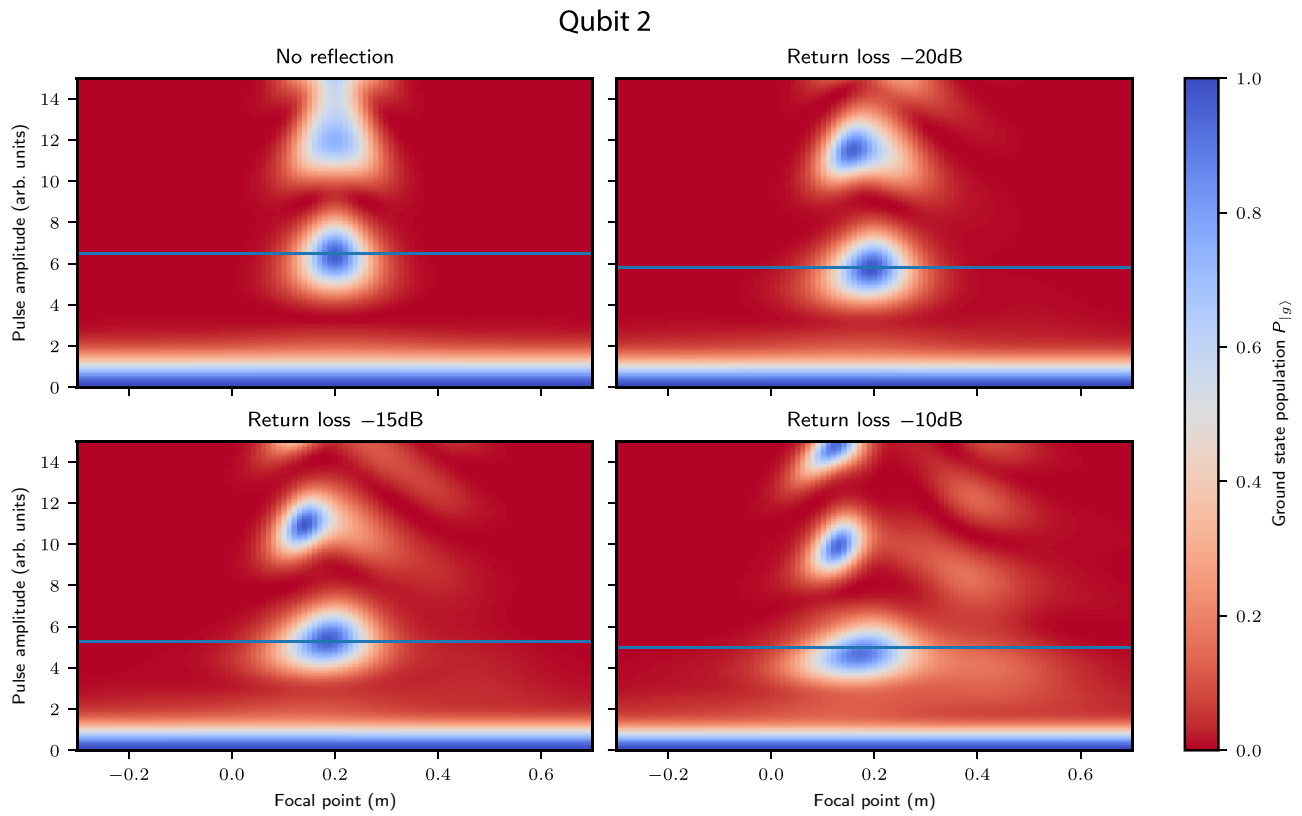


FIG. 7. Ground state population vs return loss for Q2. Simulated ground state population for a transmon at a frequency of 7.2 GHz and an anharmonicity of 420 MHz after interacting with a pulse with a focal point $z = 0$ m and a spot size of 3.5 cm. The different panels show different amplitudes of the parasitic reflection. The reflection considered is constant for all frequencies, and the source of the reflection is 5 cm from the qubit.

medium (in our case a vacuum). The dispersion relation is used to compute the central k vector of pulse, given by $k_0 = \sqrt{\omega_{ge}^2/c^2 - k_c^2}$, where ω_{ge} is the frequency of the transition between the ground state and the first excited state of the transmons. Note that the extension of this theoretical description to other systems can be done by changing the dispersion relation $\omega(k)$.

The time-dependent electric field in Eq. (A3) corresponds to the pulse at the focal point, where all the k components of the pulse are in phase and the maximum amplitude is present. The equation to backpropagate the pulse to arbitrary locations along the waveguide reads

$$E(t,z,d_f) = \frac{1}{2\pi}\int_{-\infty}^{\infty} \mathrm{d}\omega e^{i\omega t} \times \left[\int_{-\infty}^{\infty} \mathrm{d}t' e^{-i\omega t'} E_f(t')\right] e^{i\mathrm{sgn}(\omega)k(\omega)(z-d_f)}, \quad \text{(A4)}$$

where $k(\omega) = \sqrt{\omega^2 - \omega_c^2}/c$ and the sign function ensures that $E(t,z,d_f)$ is real. Physically, the sign function corresponds to a wave that propagates in only one direction (toward increasing z). The input of the rectangular waveguide is used as the origin of the z axis. Therefore, the input waveform is computed with Eq. (A4) by setting our $z = 0$.

To gain intuition on the interaction between a quantum emitter and the self-focusing pulse described by Eq. (A4), we perform two approximations. First, we consider the quantum emitter to be a two-level system, instead of a transmon with multiple levels of energy. Second, we apply the rotating-wave approximation, which implies that the Rabi frequency (proportional to the field amplitude) is small compared with the qubit frequency. In that case, the Hamiltonian that describes the qubit dynamics can be written in the rotating frame as

$$\frac{\hat{H}_{\mathrm{LZ}}}{\hbar} = \Delta(t,z)\hat{\sigma}_z + \frac{g(t,z)}{2}\left(\hat{\sigma}_+ + \hat{\sigma}_-\right), \quad \text{(A5)}$$

where $\Delta(t,z)$ is the qubit detuning, $g(z,t)$ is the Rabi coupling, and z is the position of the qubit. Both $\Delta(t,z)$ and $g(z,t)$ can be computed from the analytical representation of the pulse electric field $E(t,z) = A(t,z)\exp(i\phi(t,z))$, where $A(t,z)$ is the instantaneous amplitude and $\phi(t,z)$ is the instantaneous phase of the pulse. In particular, the qubit detuning is given by $\Delta(t,z) = \omega_q - (\partial\phi/\partial t)(t,z)$, where

ω_q is the qubit frequency and $(\partial\phi/\partial t)(t,z)$ is the instantaneous frequency of the pulse. The Rabi coupling is given by $g(t,z=z) = d_{eg}A(t,z)$, where d_{eg} is the electric dipole moment of the qubit, corresponding to the coupling of the first transition of the qubit to the waveguide.

In Fig. 5(a), we show the energy of the dressed states of the qubit as a function of the instantaneous detuning $\Delta(t,z)$. The dressed states are separated by an energy gap, as in the case of the usual Landau-Zener process. However, here both the detuning and the amplitude are time dependent and position dependent, due to the interplay between the chirping and the amplitude of the pulse for different qubit positions. When the pulse has not yet reached the qubit, the energy gap is closed and the qubit is in a specific dressed state. As the pulse interacts with the qubit, the energy gap opens, and the qubit detuning changes, causing the qubit to adiabatically follow the evolution of the dressed state. Specifically, if a qubit, initially prepared in the ground state, is placed at the focal point of the pulse, it is excited and subsequently de-excited. Conversely, if the qubit is not at the focal point, it remains excited after interacting with the pulse, as the energy gap closes while the qubit is excited.

Figures 5(b) and 5(c) show the energies of the dressed states as a function of time for different experimental conditions—namely, for different strengths of the Rabi coupling and different positions of the qubit. Specifically, Fig. 5(b) shows the energies of the dressed states as a function of time for a qubit placed at the focal point. Here we see that the energy of the dressed state is symmetric, and has three low-energy parts, corresponding to the instances in which the qubit is in the ground state (initial), in the excited state (at half the interaction time), and in the ground state (after the interaction with the pulse) again. There exists an optimal value of the Rabi coupling amplitude, such that the coupling is large enough so that the energy gap appears, allowing the qubit to adiabatically follow one of the dressed states. As the amplitude of the pulse increases, the rotating-wave approximation becomes less valid, as counterrotating terms and higher energy levels become significant. This explains why the dynamics described appears only for a specific pulse amplitude. In Fig. 5(c), we show the dressed state energies for different qubit positions. There, for the qubit placed out of the focal point, the eigenenergies are asymmetric, illustrating the fact that the qubit cannot transition back to the ground state.

APPENDIX B: IMPACT OF REFLECTIONS

The response of the two qubits Q1 and Q2 interacting with a self-compressing pulse is qualitatively different for each qubit, as can be observed in Fig. 2. To understand this discrepancy, we perform numerical simulations of the evolution of a transmon qubit interacting with a pulse subject to reflections at the end of the waveguide. In Figs. 6 and 7, we show the simulated populations for a single reflection 10 cm from the qubit, for three different amplitudes. The reflection is considered to be pointlike, and thus reflects every frequency with the same amplitude and phase. Additionally, we compare the simulations with the case where no parasitic reflections alter the system.

We observe that, even for moderate reflection amplitudes (with an equivalent return loss of -20 or -15 dB), the quantitative behavior of the populations of Q1 and Q2 are significantly different. In Fig. 2(a), the transmission measurement through the waveguide shows several decibels of amplitude changes for about 500 MHz above the cutoff, which indicates a nonoptimal return loss due to impedance mismatches. This effect is due to the rectangular waveguide to coaxial cable adapters, which are operated out of the specification regime (the WR90 waveguide is usually operated between 8.20 and 12.40 GHz). Moreover, this main reflection is superimposed with multiple reflections originating from other microwave elements (such as cable or microwave components), which by themselves have specific frequency-dependent responses. The superposition of multiple reflections considerably complicates the dynamics of the qubits, as the exact temporal shape of the pulse affects the qubit state. We observe that Q1 (see Figs. 6 and 8) is more affected by reflections than Q2 (see Figs. 7 and 8), due to the longer round-trip distance that the reflected pulse travels before returning to Q1.

To accurately simulate the system with real experiment reflections, one would need to measure the scattering matrix and compute the impulse response from the qubit for the relevant frequency. One would then be able to compute the electric field at the qubit location as a function of time and obtain its dynamics. It is challenging to do this accurately at room temperature, and is practically unfeasible at cryogenic temperatures. However, for simplicity we instead illustrate the impact of a simple broadband reflection on a qubit. With only a single reflection, we already observe a strong change in the state of the qubit. Frequency-dependent reflection leads to a more complicated response, which could better explain the differences in the experimental behavior of the two qubits.

APPENDIX C: SELF-FOCUSING PULSE CALIBRATION

The self-focusing pulse effect is dependent on both the focal point and the pulse amplitude. In Fig. 9 we characterize the effect of both the pulse focal point d_f and the pulse amplitude, set by the voltage at the waveform generator. For small pulse amplitudes both qubits remain mainly in the ground state (blue region close to the x axis). When the pulse amplitude is increased, we observe that most of the qubit population remains in the ground state only if the focal point of the pulse coincides with the position of the

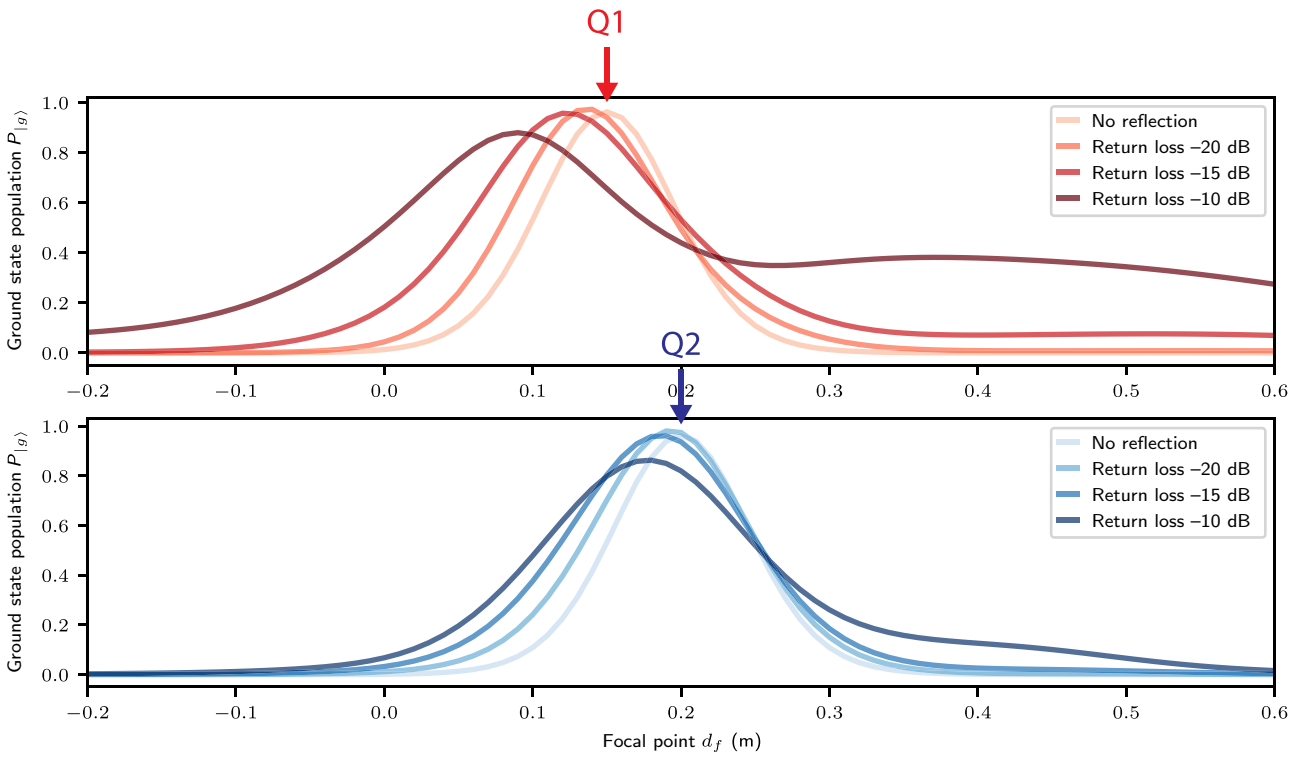


FIG. 8. Ground state population vs return loss for Q1 and Q2. Simulated line-cuts of the ground state population for Q1, indicated in Fig. 6, and for Q2, indicated in Fig. 7.

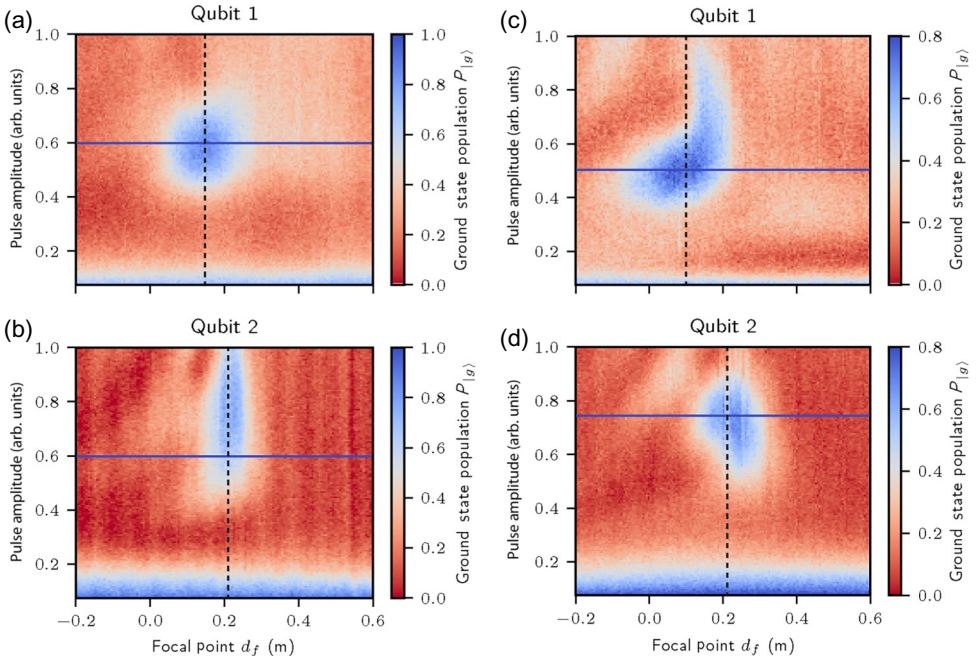


FIG. 9. Self-focusing pulse calibration. The amplitude and focal point of the self-focusing pulses are swept to calibrate the optimal self-focusing effect, shown in Fig. 2. (a),(b) This experiment for either Q1 or Q2, respectively, when the other qubit is tuned out of the waveguide passband. (c),(d) This experiment when both Q1 and Q2 are tuned to the same frequency.

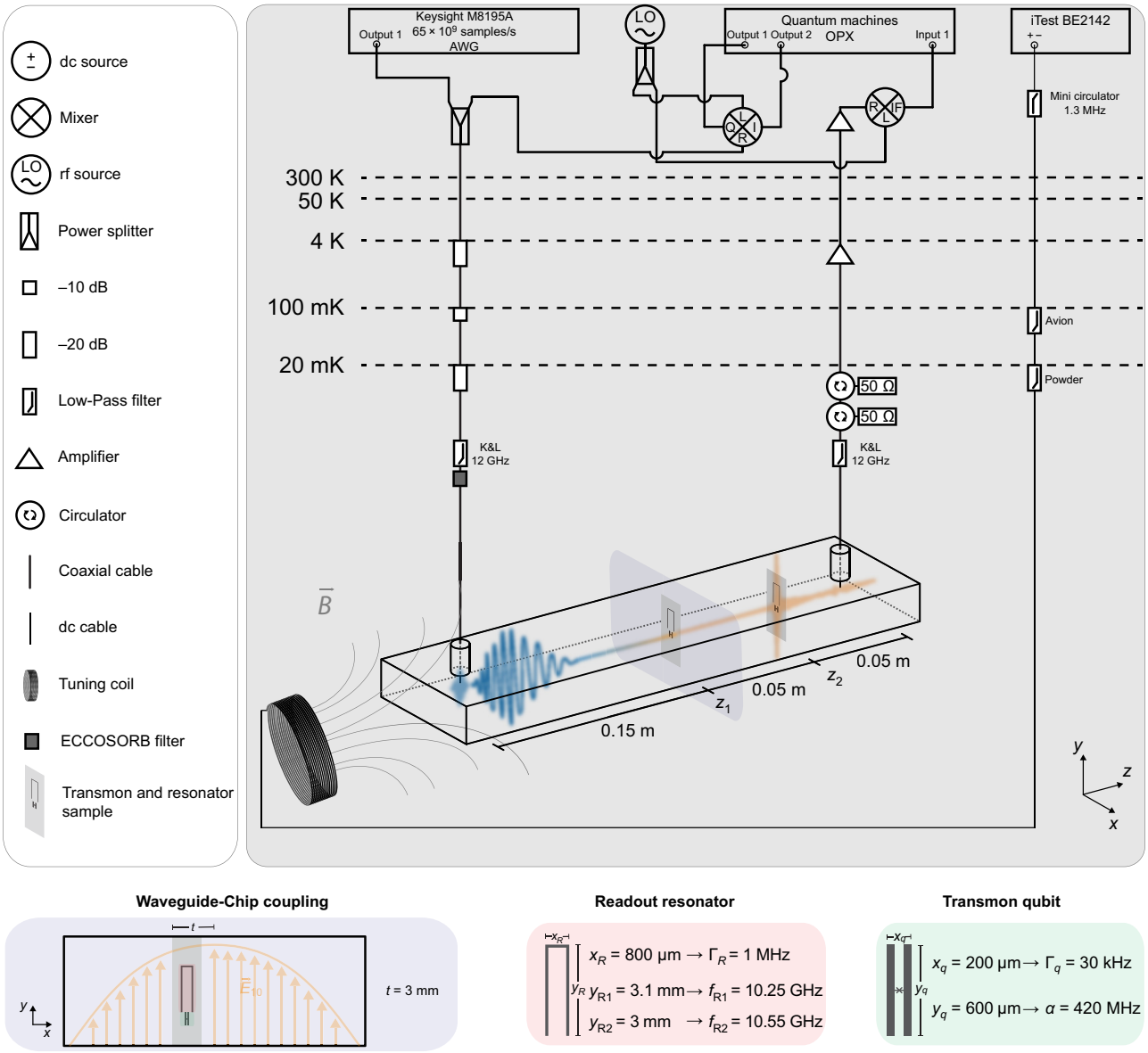


FIG. 10. Experimental wiring with selected components. Excitation and readout signals are individually generated with the Keysight AWG and Quantum Machines OPX quantum controller, respectively, and are then combined into a single input line that is connected to the waveguide sample. The waveguide output connects to the measurement setup, where the readout pulse is down-converted, and then demodulated and digitized by the OPX quantum controller. The bias coil is located at the output port such that it will supply a magnetic field that gradually decays along the z axis. L, local oscillator; R, radio frequency; I, in-phase; Q, quadrature; IF, intermediate frequency; and the LO designates a generator used for the local oscillator of the mixer.

qubit. However, for the other focal points, the ground state population decreases due to the excitation of higher states of the transmon qubit. There exists an optimal pulse amplitude where this behavior occurs, as theoretically predicted [22]. The optimal amplitude for Q1 is lower than for Q2 as it is coupled more strongly to the waveguide. In particular, for the optimal pulse amplitude, the qubit remains in the ground state for a focal point d_f of approximately 0.1 m for Q1 and approximately 0.2 m for Q2, corresponding to the positions of the qubit in the waveguide. Plots of changing focal point with constant amplitude (horizontal line-cuts in Fig. 9) are shown in Fig. 3.

APPENDIX D: EXPERIMENTAL OVERVIEW

The measurements presented in this article are performed in an Oxford Triton Cryofree dilution refrigerator

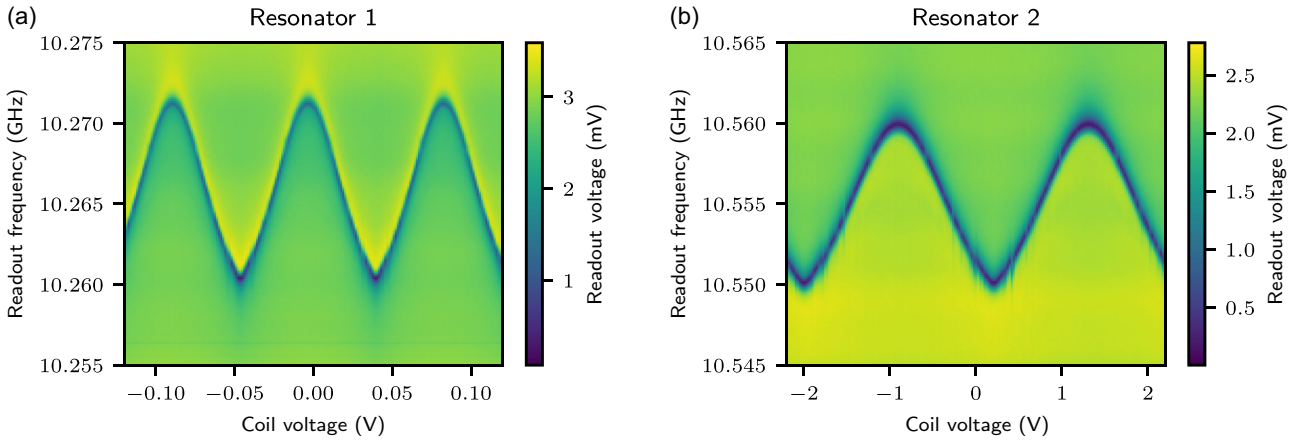


FIG. 11. Resonator spectroscopy. Transmission magnitude of a readout pulse through the waveguide when its frequency is changed and the current through a tuning coil is varied. Application of a voltage to a resistor induces a current through a coil that is mounted on the waveguide and changes the flux that threads the superconducting quantum interference device loops of the transmons. This method is used to tune the transmons' resonance frequency. Each transmon has a dispersively coupled resonator that is tuned according to the detuning between them. As the resonators are coupled directly to the waveguide, their line shape is observable by measurement of the transmission around the resonance frequencies. Resonator 2 needs roughly 20 times the voltage to tune the same amount of oscillations. Following from this we can identify resonator 1 as the chip closer to the tuning coil.

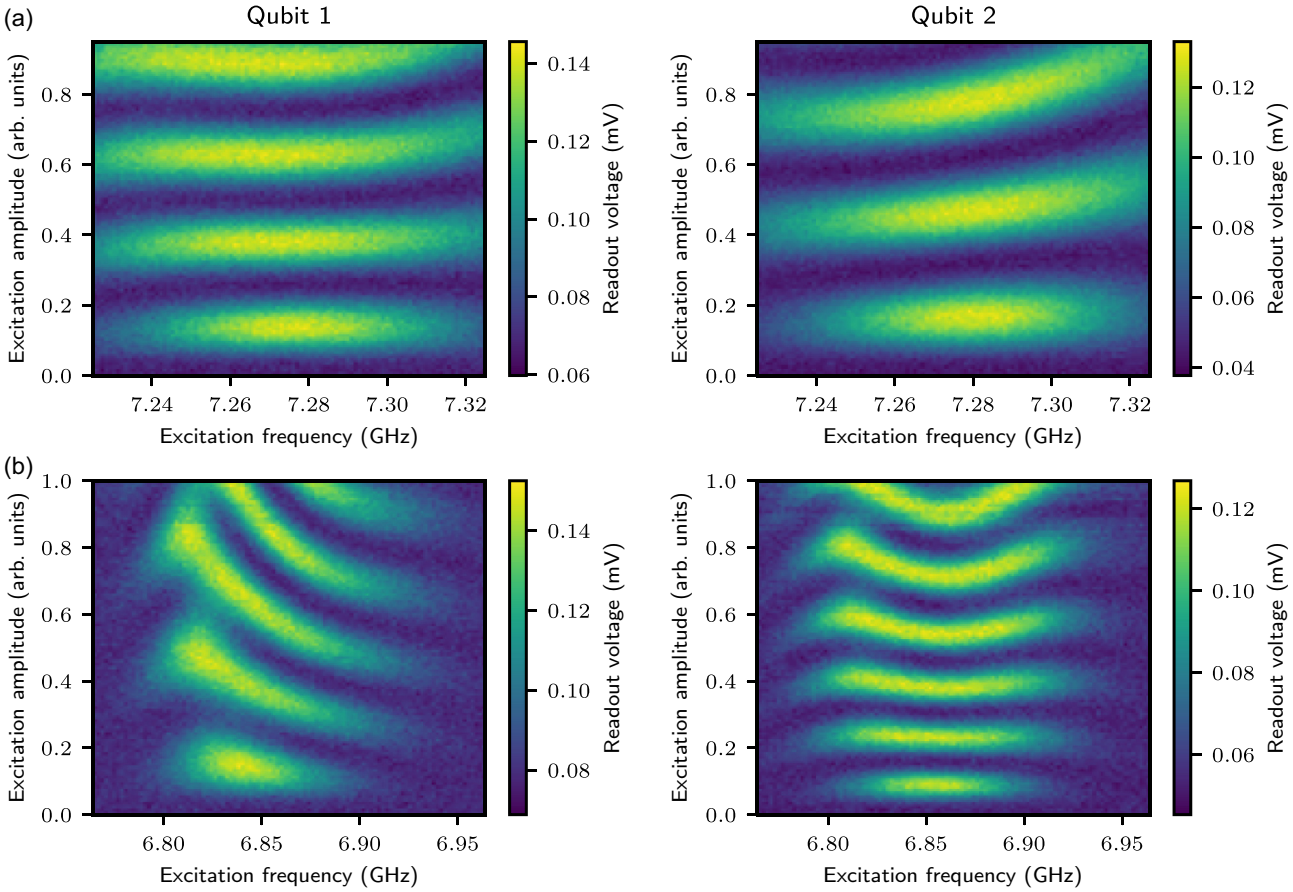


FIG. 12. Rabi oscillations. (a) We perform a Rabi experiment, increasing the amplitude of a Gaussian pulse of width $\sigma = 10\,\text{ns}$ while changing its carrier frequency. The Rabi oscillations occurring between the ground state $|g\rangle$ and the excited state $|e\rangle$ for Q1 and Q2 are used to calibrate π pulses. We attribute the asymmetry to different coupling rates between each qubit and the waveguide. (b) We repeat the experiment around the expected transition frequency of the first excited state $|e\rangle$ and the second excited state $|f\rangle$ after initializing the transmon in $|e\rangle$.

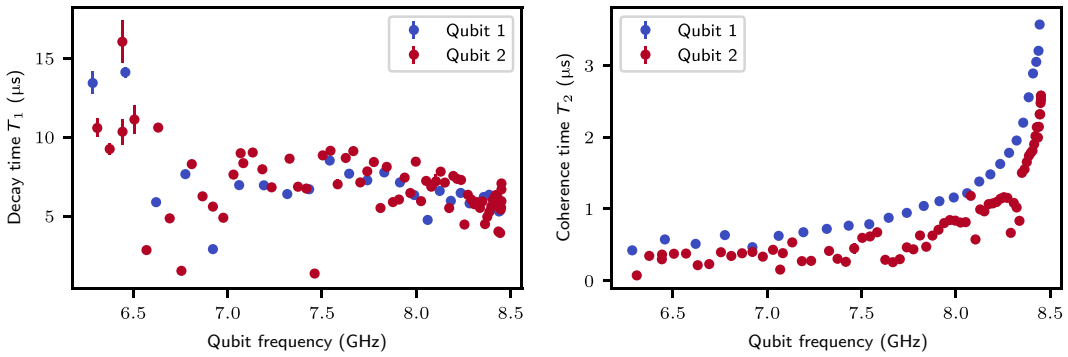


FIG. 13. Qubit decay. After initializing the qubit in the excited state $|e\rangle$ and waiting for a variable delay time, we measure the transmission through the resonator to see the characteristic exponential energy decay with time constant T_1. The decay times of both qubits are limited by the direct coupling to—and thus photon emission into—the waveguide.

system with a DU7-300 dilution unit, with base temperature $T = 20\,\text{mK}$. In Fig. 10, the dashed line at $T = 300\,\text{K}$ separates the cryostat from the room-temperature electronics. The input coaxial cables are attenuated by 20 dB at the 4 K stage, followed by 10 dB at the 100 mK stage and another 20 dB at the 20 mK stage. To allow magnetic field tuning of the transmons, the section of the rectangular waveguide containing the qubits is fabricated from oxygen-free high-purity copper, while the first half is made from aluminum. The inner dimensions (y, x, z) are $10.2 \times 22.9 \times 250\,\text{mm}^2$ (input to output coupling port). The commercial adapters at the input and output of the waveguide are impedance matched to the 50 Ω impedance of the coaxial cables to minimize reflections. The fundamental cutoff frequency $\omega_{c,10}/2\pi = 1/2a\sqrt{\mu\epsilon} = 6.546\,\text{GHz}$ depends only on the longest extension $a = 22.9\,\text{mm}$ perpendicular to the propagation direction, the vacuum permittivity ϵ, and the vacuum permeability μ. The next higher mode cutoffs of the waveguide are the TE_{20} mode at $\omega_{c,20}/2\pi = 13.091\,\text{GHz}$ and the TE_{01} mode at $\omega_{c,01}/2\pi = 14.696\,\text{GHz}$. For frequencies above the cutoff, the electromagnetic field propagates through the hollow core of the waveguide with propagation constant $\beta = \sqrt{k^2 - k_c^2}$, defined by the wave vector of the propagating mode $k = \omega\sqrt{\epsilon\mu}$ and the cutoff wave vector $k_c = \pi/a$. The phase velocity is then expressed as $v_p = \omega/\beta$. The wavelength in the waveguide is expressed as $\lambda_g = 2\pi/\beta$.

The waveguide input and output are connected to waveguide-to-coaxial-cable adapters that enable the transmission of qubit control and readout pulses from the room-temperature control electronics through the waveguide. The waveguide input is connected to a Quantum Machines OPX quantum controller, which triggers an AWG that generates the excitation pulses given in Eq. (2) with a sampling rate of 65×10^9 samples/s. The readout pulse is a single-frequency Gaussian pulse with a standard deviation σ of 100 ns, while the broadband pulse amplitude and phase are specifically shaped to focus on a given spot, resulting in a pulse bandwidth on the order of a

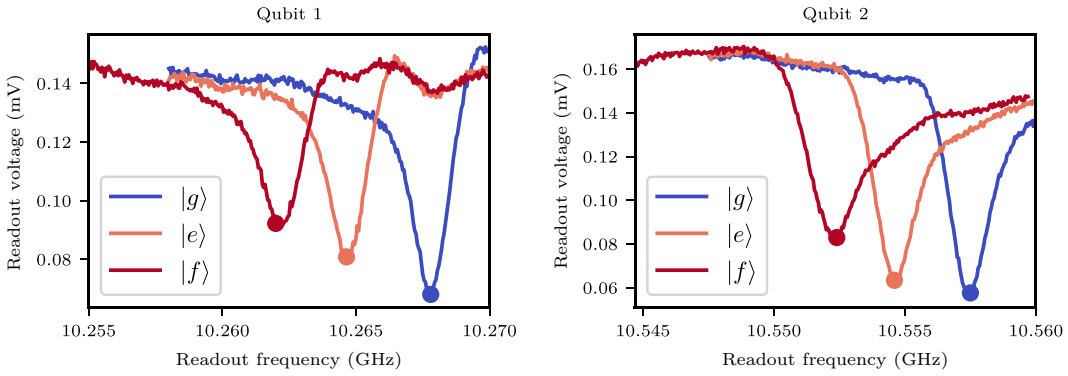


FIG. 14. Dispersive resonator shifts. We measure the transmission for frequencies around the resonators when we leave the transmon in the ground state $|g\rangle$ and excite it to the first excited state $|e\rangle$ or second excited state $|f\rangle$. As expected, the resonance frequency of the readout resonator shifts by the dispersive shift $\chi_{ge,\text{Q1}}/2\pi = 3.15\,\text{MHz}$ and $\chi_{ge,\text{Q2}}/2\pi = 2.65\,\text{MHz}$ when the qubit is prepared in the first excited state $|e\rangle$. When the qubit is prepared in the second excited state $|f\rangle$, the resonator shifts additionally by $\chi_{ef,\text{Q1}}/2\pi = 2.9\,\text{MHz}$ and $\chi_{ef,\text{Q2}}/2\pi = 2.2\,\text{MHz}$.

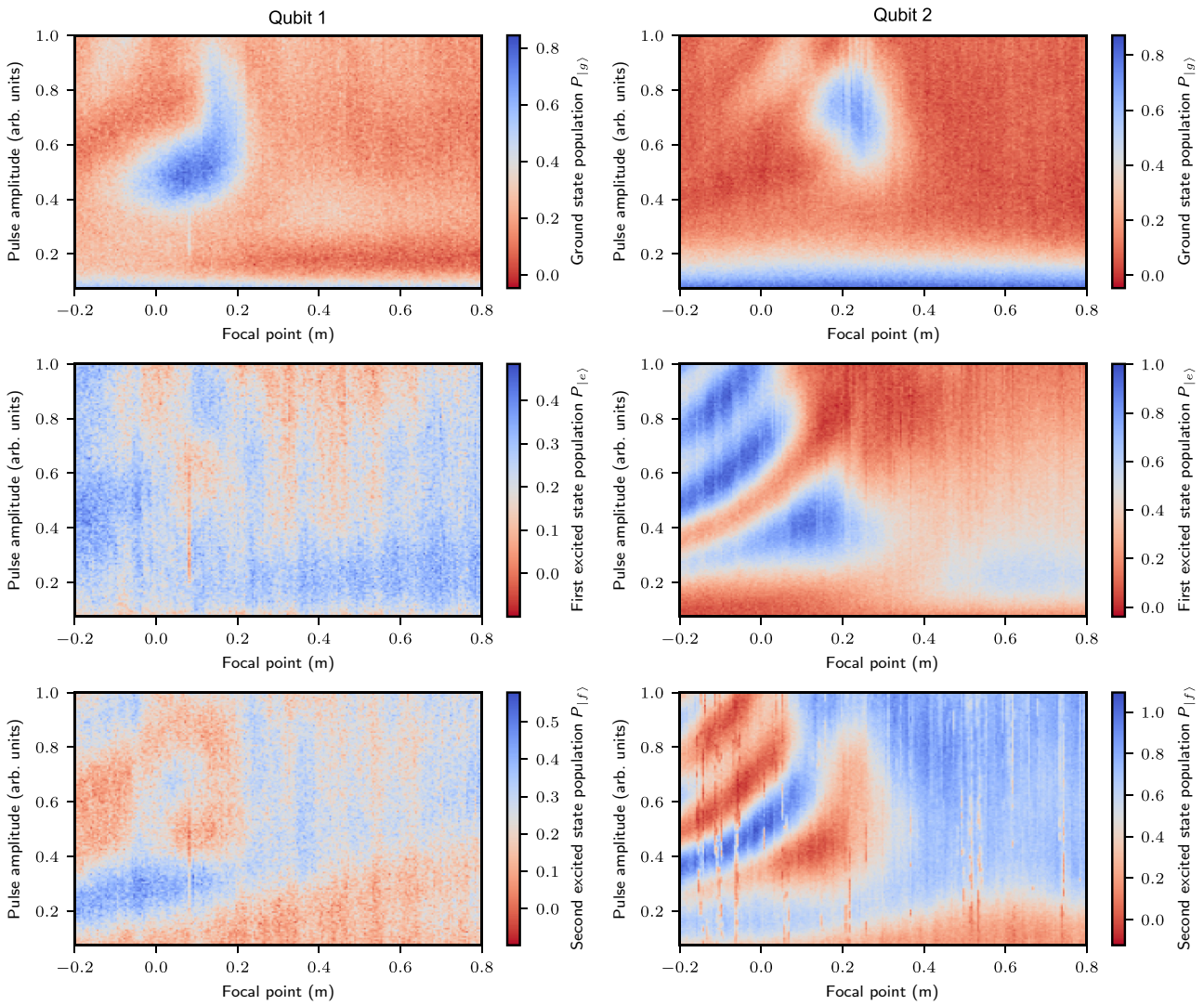


FIG. 15. State population after the focusing pulse: one qubit. The ground state population $P_{|g\rangle}$, the first exited state population $P_{|e\rangle}$, and the second excited state population $P_{|f\rangle}$ of Q1 and Q2 after interaction with the self-compressing pulse are shown. Here one qubit has been tuned below the waveguide cutoff, where it does not interact. These plots show that most of the population is transferred into the excited states when the focal point matches the physical position of each qubit.

few gigahertz. The tuning coil is connected to a voltage source (iTest BE2142) that uses a resistor with resistance $R = 1\,\mathrm{k}\Omega$ to convert the voltage into a biasing current that eventually induces a magnetic field at the qubits to change their resonance frequencies. To cancel other external magnetic fields, the waveguide sample is placed into a mu-metal and superconducting shield.

The transmon-resonator design is patterned by electron-beam lithography (Raith eLINE Plus 30 kV) on a bilayer resist stack [bottom layer 1 μm of MMA(8.5)MAA EL13, top layer 0.2 μm of 950 poly(methylmethacrylate) A4]. The substrates are sapphire wafers (diameter 50.8 mm), and therefore we sputter a thin layer of gold on top of the resist stack to avoid charging of the sample. After lithography, the gold is etched in a solution of potassium iodide with iodine and water. After development of the resist in an isopropyl alcohol and water (3:1) solution, two layers of aluminum (25 and 30 nm) are deposited with a Plassys MEB550S electron-beam evaporator. The junction barrier is formed by a controlled oxidation step before the deposition of the second layer. After lift-off, the samples are laser-diced into individual $3 \times 16\,\mathrm{mm}^2$ chips and inserted into the waveguide. They are thermalized to the base temperature by a clamp that is attached to the waveguide housing, which is screwed onto the cryostat base plate. The transmons are tunable with symmetric Josephson junctions and a maximum frequency of 8.5 GHz. The antenna of the transmon is formed by two rectangular pads of size $A_{\mathrm{pad}} = 50 \times 600\,\mu\mathrm{m}^2$ $(x \times y)$ separated by a gap d_{gap} of 100 μm and connected by the wires leading to the junctions. The

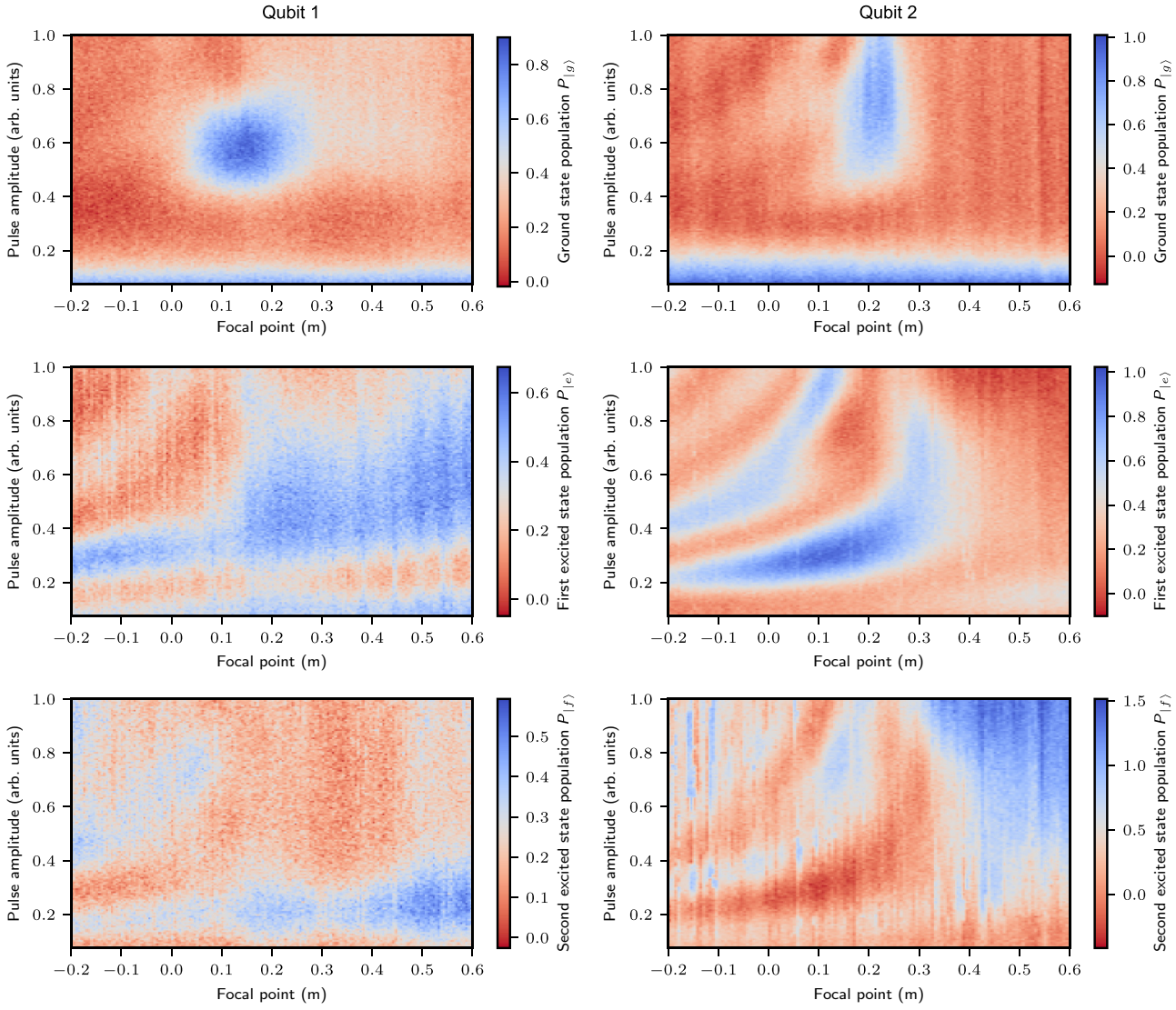


FIG. 16. State population after the focusing pulse: two qubits. The ground state population $P_{|g\rangle}$, the first excited state population $P_{|e\rangle}$, and the second excited state population $P_{|f\rangle}$ of Q1 and Q2 after interaction with the self-compressing pulse when the qubits are tuned into resonance are shown. These plots show that most of the population is transferred into the excited states when the focal point matches the qubit position.

gradient of the magnetic field supplied by the tuning coil, shown in Fig. 10, results in Q1 and Q2 being subjected to different changes in magnetic field amplitude when the current through the coil is varied. The distance between the qubits results in a stronger (for Q2) or weaker (Q1) dependence on the applied current, as shown in Fig. 11. To tune one period of Q1, we need a voltage of roughly 0.1 V, while we need almost 2 V for Q2. This enables us to detune the qubits for the single-qubit scenario or tune them into resonance for the two-qubit experiments. The resonators are patterned above the transmons, allowing us to determine the transmon state via dispersive readout [32].

The samples are embedded in the rectangular waveguide, located at $z_1 = 15\,\text{cm}$ and $z_2 = 20\,\text{cm}$, where $z = 0$ corresponds to the input port. The resulting qubit-qubit separation along the photon propagation direction corresponds to half a wavelength $d_z = 5\,\text{cm} = \lambda/2$ at a frequency f of 7.2 GHz. Each chip consists of a transmon qubit [24] that is capacitively coupled to a stripline resonator [33]. Both the qubit and the resonator antenna are perpendicular to the propagating electric field and symmetric along the x direction, and thus they would not couple to the waveguide if placed in the center. To achieve an electric field gradient across the sample and therefore couple the qubit and resonator to the waveguide, the chip is placed $t = 3\,\text{mm}$ off-center with respect to the maximum electric field amplitude, shown in the bottom-left panel in Fig. 10. The length of the transmon dipole antenna sets the transmon-waveguide coupling strength $\Gamma_q/2\pi$ to be approximately 30 kHz

such that energy relaxation is limited by the coupling to the waveguide [34]. The distance between the resonator arms is used to achieve a resonator-waveguide coupling strength $\Gamma_{R1}/2\pi = \Gamma_{R2}/2\pi$ of approximately 1 MHz. The qubit and respective resonator are capacitively coupled with a coupling strength $g/2\pi$ of approximately 250 MHz. The fundamental resonance frequencies of the readout resonators $\omega_{R1}/2\pi = 10.25$ GHz and $\omega_{R2}/2\pi = 10.55$ GHz are visible in the transmission measurement in Fig. 1(a). The detuning ensures that both transmon qubits can be read out independently.

APPENDIX E: QUBIT COUPLING

The qubits are characterized by only using conventional Gaussian waveform excitation pulses. In Fig. 12, the amplitude of the pulse is swept while its detuning is changed from the qubit frequency. The Rabi oscillations that occur between the ground state $|g\rangle$ and the excited state $|e\rangle$ for Q1 and Q2 are used to calibrate π pulses. With the calibrated π pulse, we initialize the qubit in the $|e\rangle$ state and repeat the experiment around the expected transition frequency of the first excited state $|e\rangle$ and the second excited state $|f\rangle$. The transition frequency $\omega_{ef}/2\pi$ is approximately 300 MHz above the waveguide cutoff frequency. Here the transmission varies between 70% and 100% in the measured range shown in Fig. 12, thus altering the coupling significantly. Even though the chips are designed very similarly, we also observe that Q1 is more strongly coupled to the waveguide. An explanation could be the lower frequency of the readout resonator and thus less Purcell protection by the resonator. To verify that the qubit decay time T_1 is indeed limited by coupling to the waveguide, we fit an exponential to the time decay at different frequencies, ranging from the highest possible transon resonance frequency (sweet spot) to the minimal frequency. The minimal frequency is limited by attenuation of the pulse below the cutoff. In Fig. 13 we show the measured and extracted decay time T_1 and coherence time T_2, obtained from a Ramsey experiment. The waveguide-limited decay can be experimentally verified by the tuning of the qubits below the cutoff frequency $f_c = 6.56$ GHz. The coupling decreases exponentially when we go to frequencies lower than f_c [35], and thus we observe an increase in T_1. For T_2 we observe the expected decrease when tuning the qubits away from the sweet spot. Note that the focusing experiments are performed at around 7.2 GHz. In a repetition of the experiment, we can increase T_2 by designing the sweet spot of the transmon flux susceptibility closer to the frequency where we perform the experiments.

APPENDIX F: POPULATION CALIBRATION

We measure the transmission through the waveguide QED setup to determine the state of the qubits. The resonators experience a state-dependent dispersive shift χ and enable us to distinguish between the three lowest energy levels of the transmon qubit. In Fig. 14, we plot the transmission around the resonance frequencies of the resonators, where the minimum of the resonant feature varies when we either initially excite the qubits into the first excited state $|e\rangle$ with a π pulse or the second excited state $|f\rangle$ with a π pulse followed by a π_{ef} pulse or leave the qubit in the ground state $|g\rangle$. The dots indicate the frequency that is used for the readout where the measured voltage corresponds to full population of the respective states. Decreasing amplitude for higher prepared transmon states is mostly due to decay losses during the readout. An increase in transmission amplitude thus corresponds to lower population of the measured state. To calibrate, for example, $P_{|g\rangle} = 0$, we could use the amplitude at the frequency of the resonator when the qubit is in the ground state $f_{|g\rangle}$ when we excite the qubit. However, the focusing pulse depletes the ground state much further than a conventional Gaussian excitation pulse due to the excitation into higher transmon levels, causing a cascaded decay and thus higher transmitted voltage. With use of the calibration described, this would result in negative state probabilities in Figs. 2 and 4, as well as Figs. 15 and 16. To calibrate the corresponding probability $P_{|i\rangle} = 0$ for states i, we thus use the highest measured voltages when performing the focusing experiment corresponding to Figs. 15 and 16. This underestimates the prepared state fidelities compared with the use of the calibration coming from a regular Gaussian excitation pulse but ensures positive values in the population measurements. The readout can be improved by use of higher-order state discrimination and multiplexing of readout signals, etc., but is not further considered in the article. Using the calibration routine described above, we show the population of the states $|g\rangle$, $|e\rangle$, and $|f\rangle$ for only either Q1 or Q2 tuned to $\omega_{ge}/2\pi = 7.2$ GHz in Fig. 15 or both qubits tuned to the same frequency in Fig. 16. The population of the states $|e\rangle$ and $|f\rangle$ for all focal points and pulse amplitudes completes the selected line-cuts in Figs. 2(b) and 4(b). Compared with theory, we observe a similar qualitative behavior of distorted features caused by reflections. The distance between Q2 and the output port matches $\lambda/2 = 5$ cm. Especially for the excited states, we observe many sudden changes in readout amplitude. These glitches are responsible for the state population $P_{|i\rangle}$ exceeding 1.

[1] T. Brabec and F. Krausz, Intense few-cycle laser fields: Frontiers of nonlinear optics, Rev. Mod. Phys. **72**, 545 (2000).

[2] D. M. Pozar, *Microwave Engineering* (Wiley, Hoboken, NJ, 2012), 4th ed.

[3] J. D. Joannopoulos, P. R. Villeneuve, and S. Fan, Photonic crystals: Putting a new twist on light, Nature **386**, 143 (1997).

[4] A. S. Sheremet, M. I. Petrov, I. V. Iorsh, A. V. Poshakinskiy, and A. N. Poddubny, Waveguide quantum electrodynamics: Collective radiance and photon-photon correlations, Rev. Mod. Phys. **95**, 015002 (2023).

[5] S. J. Masson and A. Asenjo-Garcia, Atomic-waveguide quantum electrodynamics, Phys. Rev. Res. **2**, 043213 (2020).

[6] O. Astafiev, A. M. Zagoskin, A. A. Abdumalikov, Y. A. Pashkin, T. Yamamoto, K. Inomata, Y. Nakamura, and J. S. Tsai, Resonance fluorescence of a single artificial atom, Science **327**, 840 (2010).

[7] A. F. van Loo, A. Fedorov, K. Lalumière, B. C. Sanders, A. Blais, and A. Wallraff, Photon-mediated interactions between distant artificial atoms, Science **342**, 1494 (2013).

[8] M. Zanner, T. Orell, C. M. F. Schneider, R. Albert, S. Oleschko, M. L. Juan, M. Silveri, and G. Kirchmair, Coherent control of a multi-qubit dark state in waveguide quantum electrodynamics, Nat. Phys. **18**, 538 (2022).

[9] I.-C. Hoi, C. M. Wilson, G. Johansson, T. Palomaki, B. Peropadre, and P. Delsing, Demonstration of a single-photon router in the microwave regime, Phys. Rev. Lett. **107**, 073601 (2011).

[10] B. Kannan, D. L. Campbell, F. Vasconcelos, R. Winik, D. K. Kim, M. Kjaergaard, P. Krantz, A. Melville, B. M. Niedzielski, J. L. Yoder, T. P. Orlando, S. Gustavsson, and W. D. Oliver, Generating spatially entangled itinerant photons with waveguide quantum electrodynamics, Sci. Adv. **6**, eabb8780 (2020).

[11] N. M. Sundaresan, R. Lundgren, G. Zhu, A. V. Gorshkov, and A. A. Houck, Interacting qubit-photon bound states with superconducting circuits, Phys. Rev. X **9**, 011021 (2019).

[12] S. Storz, *et al.*, Loophole-free Bell inequality violation with superconducting circuits, Nature **617**, 265 (2023).

[13] B. Kannan, M. J. Ruckriegel, D. L. Campbell, A. Frisk Kockum, J. Braumüller, D. K. Kim, M. Kjaergaard, P. Krantz, A. Melville, B. M. Niedzielski, A. Vepsäläinen, R. Winik, J. L. Yoder, F. Nori, T. P. Orlando, S. Gustavsson, and W. D. Oliver, Waveguide quantum electrodynamics with superconducting artificial giant atoms, Nature **583**, 775 (2020).

[14] A. Rosario Hamann, C. Müller, M. Jerger, M. Zanner, J. Combes, M. Pletyukhov, M. Weides, T. M. Stace, and A. Fedorov, Nonreciprocity realized with quantum nonlinearity, Phys. Rev. Lett. **121**, 123601 (2018).

[15] B. Kannan, A. Almanakly, Y. Sung, A. Di Paolo, D. A. Rower, J. Braumüller, A. Melville, B. M. Niedzielski, A. Karamlou, K. Serniak, A. Vepsäläinen, M. E. Schwartz, J. L. Yoder, R. Winik, J. I.-J. Wang, T. P. Orlando, S. Gustavsson, J. A. Grover, and W. D. Oliver, On-demand directional microwave photon emission using waveguide quantum electrodynamics, Nat. Phys. **19**, 394 (2023).

[16] C. Joshi, F. Yang, and M. Mirhosseini, Resonance fluorescence of a chiral artificial atom, Phys. Rev. X **13**, 021039 (2023).

[17] E. Kim, X. Zhang, V. S. Ferreira, J. Banker, J. K. Iverson, A. Sipahigil, M. Bello, A. González-Tudela, M. Mirhosseini, and O. Painter, Quantum electrodynamics in a topological waveguide, Phys. Rev. X **11**, 011015 (2021).

[18] A. González-Tudela, C.-L. Hung, D. E. Chang, J. I. Cirac, and H. J. Kimble, Subwavelength vacuum lattices and atom–atom interactions in two-dimensional photonic crystals, Nat. Photonics **9**, 320 (2015).

[19] P. Lodahl, A. Floris van Driel, I. S. Nikolaev, A. Irman, K. Overgaag, D. Vanmaekelbergh, and W. L. Vos, Controlling the dynamics of spontaneous emission from quantum dots by photonic crystals, Nature **430**, 654 (2004).

[20] R. W. Boyd, S. G. Lukishova, Y. Shen, and C. Ascheron, eds., *Self-focusing: Past and Present: Fundamentals and Prospects*, Topics in Applied Physics, Vol. 114 (Springer, New York, NY, 2009).

[21] F. Krausz and M. Ivanov, Attosecond physics, Rev. Mod. Phys. **81**, 163 (2009).

[22] S. Casulleras, C. Gonzalez-Ballestero, P. Maurer, J. J. García-Ripoll, and O. Romero-Isart, Remote individual addressing of quantum emitters with chirped pulses, Phys. Rev. Lett. **126**, 103602 (2021).

[23] S. J. Orfanidis, *Electromagnetic Waves and Antennas* (Rutgers University, New Jersey, 2014).

[24] J. Koch, T. M. Yu, J. Gambetta, A. A. Houck, D. I. Schuster, J. Majer, A. Blais, M. H. Devoret, S. M. Girvin, and R. J. Schoelkopf, Charge-insensitive qubit design derived from the Cooper pair box, Phys. Rev. A **76**, 042319 (2007).

[25] K. Lalumière, B. C. Sanders, A. F. van Loo, A. Fedorov, A. Wallraff, and A. Blais, Input-output theory for waveguide QED with an ensemble of inhomogeneous atoms, Phys. Rev. A **88**, 043806 (2013).

[26] V. E. Manucharyan, J. Koch, L. I. Glazman, and M. H. Devoret, Fluxonium: Single Cooper-pair circuit free of charge offsets, Science **326**, 113 (2009).

[27] J. D. Brehm, A. N. Poddubny, A. Stehli, T. Wolz, H. Rotzinger, and A. V. Ustinov, Waveguide bandgap engineering with an array of superconducting qubits, npj Quantum Mater. **6**, 1 (2021).

[28] A. V. Poshakinskiy, J. Zhong, and A. N. Poddubny, Quantum chaos driven by long-range waveguide-mediated interactions, Phys. Rev. Lett. **126**, 203602 (2021).

[29] G. Wolfowicz, F. J. Heremans, C. P. Anderson, S. Kanai, H. Seo, A. Gali, G. Galli, and D. D. Awschalom, Quantum guidelines for solid-state spin defects, Nat. Rev. Mater. **6**, 906 (2021).

[30] E. Vetsch, D. Reitz, G. Sagué, R. Schmidt, S. T. Dawkins, and A. Rauschenbeutel, Optical interface created by laser-cooled atoms trapped in the evanescent field surrounding an optical nanofiber, Phys. Rev. Lett. **104**, 203603 (2010).

[31] https://zenodo.org/records/15827802.

[32] M. Boissonneault, J. M. Gambetta, and A. Blais, Nonlinear dispersive regime of cavity QED: The dressed dephasing model, Phys. Rev. A **77**, 060305 (2008).

[33] D. Zoepfl, P. R. Muppalla, C. M. F. Schneider, S. Kasemann, S. Partel, and G. Kirchmair, Characterization of low loss microstrip resonators as a building block for circuit QED in a 3D waveguide, AIP Adv. **7**, 085118 (2017).

[34] M. Dalmonte, S. I. Mirzaei, P. R. Muppalla, D. Marcos, P. Zoller, and G. Kirchmair, Realizing dipolar spin models with arrays of superconducting qubits, Phys. Rev. B **92**, 174507 (2015).

[35] Y. Liu and A. A. Houck, Quantum electrodynamics near a photonic bandgap, Nat. Phys. **13**, 48 (2017).